CellPress

Neuron
Article

Dendritic Spikes Induce Ripples in Parvalbumin Interneurons during Hippocampal Sharp Waves

Balázs Chiovini,[1,2,7] Gergely F. Turi,[1,6,7] Gergely Katona,[1] Attila Kaszás,[1,2] Dénes Pálfi,[1,2] Pál Maák,[3] Gergely Szalay,[1] Mátyás Forián Szabó,[2,4] Gábor Szabó,[5] Zoltán Szadai,[1] Szabolcs Káli,[2,4] and Balázs Rózsa[1,2,*]

[1]Two-Photon Imaging Center, Institute of Experimental Medicine, Hungarian Academy of Sciences, Budapest 1083, Hungary
[2]Faculty of Information Technology and Bionics, Pázmány Péter Catholic University, Budapest 1083, Hungary
[3]Department of Atomic Physics, Budapest University of Technology and Economics, Budapest 1111, Hungary
[4]Laboratory of Cerebral Cortex Research, Institute of Experimental Medicine, Hungarian Academy of Sciences, Budapest 1083, Hungary
[5]Transgenic Facility, Institute of Experimental Medicine, Hungarian Academy of Sciences, Budapest 1083, Hungary
[6]Department of Neuroscience, Columbia University, New York, NY 10032, USA
[7]Co-first author
*Correspondence: rozsabal@koki.hu
http://dx.doi.org/10.1016/j.neuron.2014.04.004

SUMMARY

Sharp-wave ripples are transient oscillatory events in the hippocampus that are associated with the reactivation of neuronal ensembles within specific circuits during memory formation. Fast-spiking, parvalbumin-expressing interneurons (FS-PV INs) are thought to provide fast integration in these oscillatory circuits by suppressing regenerative activity in their dendrites. Here, using fast 3D two-photon imaging and a caged glutamate, we challenge this classical view by demonstrating that FS-PV IN dendrites can generate propagating Ca^{2+} spikes during sharp-wave ripples. The spikes originate from dendritic hot spots and are mediated dominantly by L-type Ca^{2+} channels. Notably, Ca^{2+} spikes were associated with intrinsically generated membrane potential oscillations. These oscillations required the activation of voltage-gated Na^{+} channels, had the same frequency as the field potential oscillations associated with sharp-wave ripples, and controlled the phase of action potentials. Furthermore, our results demonstrate that the smallest functional unit that can generate ripple-frequency oscillations is a segment of a dendrite.

INTRODUCTION

In the hippocampus, sharp-wave ripples (SPW-Rs) are transient oscillatory events that reflect synchronized population discharges corresponding to the reactivation of previously established cell assemblies and play a crucial role in establishing long-term memory traces in the neocortex (Buzsáki, 2010; Buzsáki and Silva, 2012; Girardeau et al., 2009; Lorenz et al., 2012). According to the current model of hippocampal SPW activity, first a transient increase in pyramidal cell firing is generated autonomously in CA3 and this drives a widespread depolarization in both pyramidal cells and interneurons in CA1, leading to the generation of network ripple oscillations (Buzsáki and Silva, 2012; Traub and Bibbig, 2000). The precisely timed and anatomically structured input activity of CA3 neurons is nonlinearly transformed to neuronal output by the somatic and dendritic compartments of downstream neurons (Katona et al., 2011; Larkum et al., 2009; Losonczy and Magee, 2006). Nonlinear dendritic processing is achieved mainly by voltage-gated ion channels, which interact through locally propagating and attenuating membrane potential fluctuations; in this way, dendritic signal integration can be clustered in small (~10 μm) dendritic computational subunits ("hot spots") (Katona et al., 2011; Polsky et al., 2004). When more synaptic inputs are activated in synchrony, voltage-gated ion channels can also induce more global signals, i.e., regenerative dendritic spikes (Larkum et al., 2009; Schiller et al., 2000; Stuart et al., 1999). The relationship between network ripple oscillations, SPWs, and dendritic hot spot activity has not yet been investigated; nevertheless, several facts suggest that SPW-R-associated cell assemblies can activate dendritic hot spots. First, synchronized cell assemblies have been shown to activate dendritic hot spots (Kleindienst et al., 2011; Makino and Malinow, 2011; Takahashi et al., 2012), and during an SPW-R event up to 10% of the total neuronal population discharges in the hippocampus, making SPW-Rs the most synchronized cell assembly pattern in the cortex (Buzsáki, 2010; Buzsáki and Chrobak, 2005). Second, synaptic inputs in dendritic hot spots have been reported to be locally synchronized for an interval of ~60 ms (Takahashi et al., 2012), which matches the average length of individual SPW-R events (Buzsáki and Silva, 2012). However, whether and how these SPW-R-associated cell assemblies activate dendritic hot spots, and if this activation changes the dendritic computation and action potential output of individual neurons, have not been investigated yet.

Although many different types of cells are recruited during SPW-R events, hippocampal FS-PV INs are substantially more active than other neuron types and their firing is strongly phase-locked to network ripple oscillations (Bähner et al., 2011; Klausberger et al., 2003). It has been suggested that

FS-PV INs play key roles in the generation of SPW-Rs and during other synchronized cell assembly activities (Buzsáki and Silva, 2012; Lapray et al., 2012; Sohal et al., 2009; Taxidis et al., 2012; Tukker et al., 2013). According to the generally accepted view, FS-PV INs act in cortical circuits as fast and, essentially, passive integrators of synaptic inputs (Buhl et al., 1996; Glickfeld and Scanziani, 2006; Hu et al., 2010; Pouille and Scanziani, 2004). Under conditions of low network activity, when the incoming synaptic activity is low, the passive and active characteristics of FS-PV INs result in accelerated kinetics of excitatory postsynaptic potentials (EPSPs), a reduced, submillisecond temporal window for dendritic integration, and precise and fast coupling between EPSPs and action potential (AP) outputs (Fricker and Miles, 2000; Goldberg et al., 2003b; Goldberg and Yuste, 2005; Hu et al., 2010; Pouille and Scanziani, 2004). Ca^{2+} dynamics in the aspiny dendrites of FS-PV INs has also been found to be fast and confined to small, ~1 μm long, dendritic microdomains (Goldberg et al., 2003a; Goldberg and Yuste, 2005; Topolnik, 2012). Moreover, it has not been possible to evoke regenerative dendritic spikes in these cells, and back-propagating action potentials are severely attenuated (Goldberg et al., 2003b; Hu et al., 2010). However, under physiological high-activity conditions such as SPW-Rs, when neurons are bombarded with precisely timed dendritic inputs, the rules of dendritic integration and EPSP-AP coupling can be different (Chiovini et al., 2010; Katona et al., 2011).

Here, using high-speed, 3D, two-photon scanning in combination with electrophysiological recordings, and employing a caged glutamate compound (DNI-glutamate•TFA), we show that the classical view of the operation and functional role of FS-PV INs in cortical circuits is incorrect when these cells are activated by large synchronous cell assemblies. We demonstrate SPW-Rs can generate a transition in FS-PV INs from the well-documented ground state of passive integration to an active state, where dendritic processing and the input-output transformation of these neurons are fundamentally different. Moreover, our data suggest a mechanism for the generation of SPW-Rs by demonstrating that the smallest functional units that can generate ripple-frequency oscillations in the brain are short (~20 μm) segments of FS-PV IN dendrites.

RESULTS

Fast 3D Recording Resolves SPW-R-Associated Dendritic Input Patterns

In order to test the suggested network activity-related dynamic switch in FS-PV IN functions, we performed a variant of 3D fast acousto-optical (3D-AO) trajectory scanning (Katona et al., 2012) and combined it with simultaneous local field potential (LFP) and whole-cell patch-clamp recordings in a dual-superfusion recording chamber (Chiovini et al., 2010; Hájos et al., 2009; Katona et al., 2011). This approach allowed access to multiple, long, thin, tortuous apical dendritic segments (up to 700 μm in length) (Figure 1 and Figure S1 available online) (Katona et al., 2012) that are otherwise not accessible for in vivo recordings or dendritic patch-clamp recording. Under our recording conditions, SPW events occurred spontaneously at a rate of 1.44 ± 0.09 Hz (n = 32) and were associated with network ripple oscillations (f_{max} 249.2 ± 12.7 Hz) (Experimental Procedures; Figures 2A–2D; Movie S1) (Chiovini et al., 2010; Hájos et al., 2009). Importantly, the observed spontaneous SPW-Rs had similar laminar profiles, oscillation frequencies, and hippocampal propagation properties to those observed in vivo (Buzsáki, 1986; Hájos et al., 2009; Maier et al., 2011).

Enhanced GFP-expressing FS-PV INs (Meyer et al., 2002) in CA1 stratum pyramidale were identified with two-photon imaging and were filled with a fluorescent Ca^{2+} indicator (OGB-1 or Fluo-4) and, in some experiments, the red structure dye Alexa 594 via a somatic recording pipette. All of the recorded neurons were characterized as typical fast-spiking interneurons according to previous classifications (Table S1) (Avermann et al., 2012; Buhl et al., 1996; Hu et al., 2010; Lamsa et al., 2007). Cluster analysis further supported the homogeneity of the sampled interneuron population (see Supplemental Experimental Procedures). For 3D Ca^{2+} imaging, a reference z stack was taken with 3D-AO imaging in order to select multiple, long dendritic segments covering the majority of the dendritic arbor. Then we performed simultaneous fast 3D trajectory scanning (Katona et al., 2012) along multiple dendritic segments during spontaneous SPW-Rs (Figure 1A; Movie S1). Three-dimensional responses were spatially normalized, then projected and plotted in 2D (3D Ca^{2+} responses) (Equations S1 and S2 in the Supplemental Experimental Procedures; Figures 1B and S1A). The amplitude of the dendritic 3D Ca^{2+} responses, elicited by bAPs (five APs, 40 Hz) between two spontaneous SPW-R events, decreased rapidly as a function of distance, dropping below the detection threshold at 113.88 ± 14.50 μm from the soma (n = 13; Figures 1C and S1; Movie S2), consistent with recently published data (Chiovini et al., 2010; Hu et al., 2010). These data can be explained by the passive properties of FS-PV IN dendrites, which are dampened by a high K^+ to Na^+ conductance ratio (Hu et al., 2010; Nörenberg et al., 2010).

In contrast to somatically evoked bAPs, the amplitude of dendritic 3D Ca^{2+} responses occurring during spontaneous SPW-R-associated APs (termed SPW-APs) progressively increased as a function of distance from the soma (Figure 1C; Movie S3). Moreover, a similar, incremental response could be measured during somatically subthreshold events when spontaneous SPW-R activity did not induce any somatic APs (termed SPW-EPSP) (Figure 1; Movie S4) and the 3D Ca^{2+} response was close to zero at the soma, suggesting a dendritic rather than somatic origin for these signals (Figures 1B and 1C). Interestingly, SPW-EPSP-associated network activity that induced locally clustered responses, termed dendritic hot spots (full-width at half-maximum [FWHM]: 3.73 ± 0.13 μm) (Figures S3A–S3D), was also able to generate more generalized signals, which invaded continuous dendritic segments of the distal apical, but not the basal dendritic arbor (Figures 1B and 1D). The distance-dependent distribution of 3D Ca^{2+} responses to bAPs and to SPW-EPSPs showed a reciprocal pattern and combined to give a large and more evenly distributed 3D Ca^{2+} response in dendrites when APs were combined with SPW-EPSPs to generate SPW-APs (Figure 1C). These data suggest that network activity during SPW-Rs can shift the dendritic integration status of FS-PV INs from ground state where dendrites are passive to an "excited" state where regenerative dendritic activity, such

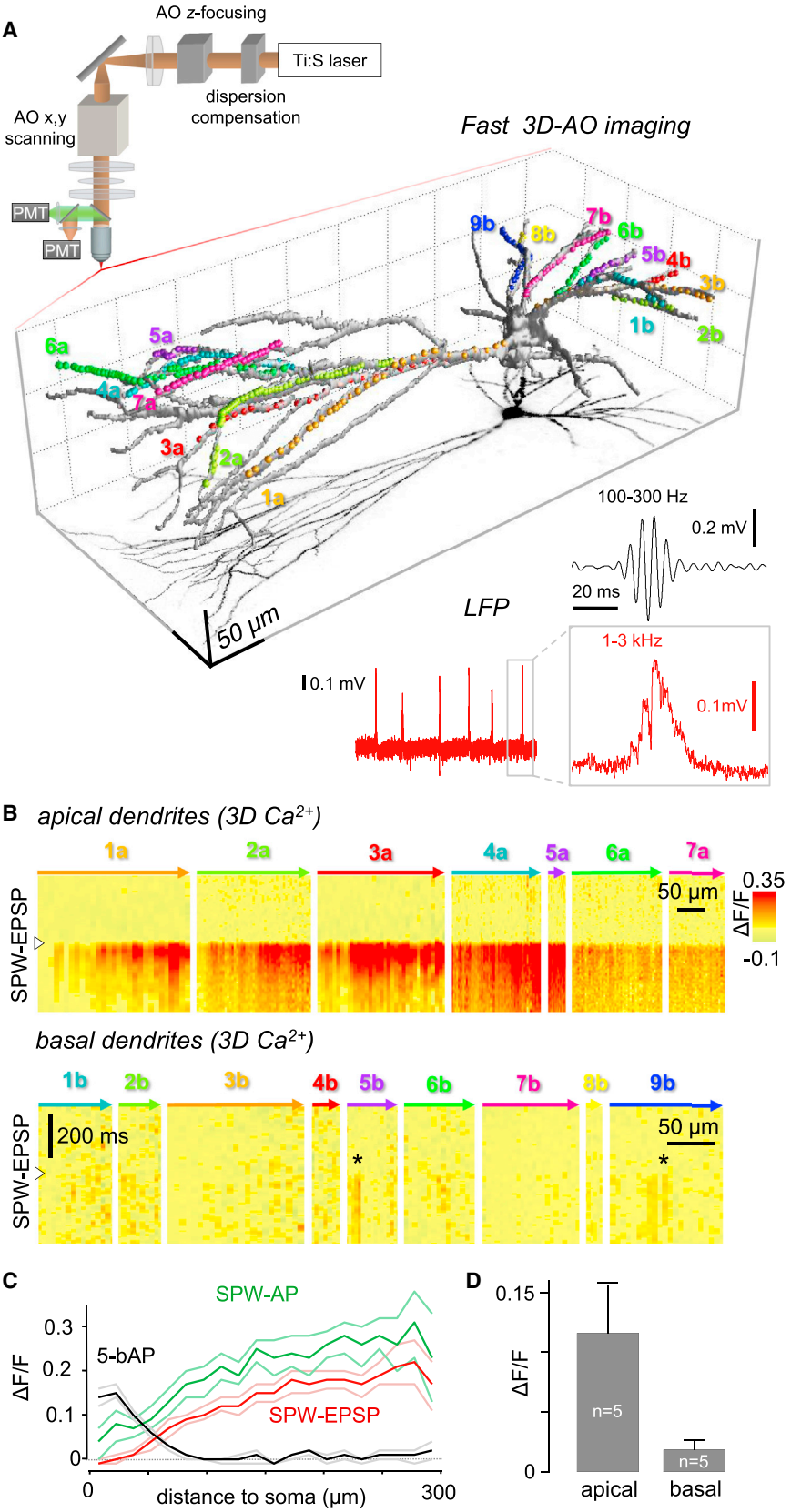

Figure 1. SPW-Associated Dendritic Spikes Revealed by Fast 3D-AO Imaging in Thin Distal Dendrites of FS-PV INs

(A) Full dendritic arborization of an FS-PV IN imaged by 3D-AO scanning in the hippocampal CA1 region. Colored spheres represent locations selected for 3D trajectory scanning. Top inset: block diagram of the 3D microscope with AO modules for fast z and lateral scanning. Right inset: representative LFP recording from str. pyramidale with six spontaneous SPW-R events (red). The last event is shown on an extended scale in two different frequency bands.

(B) SPW-EPSPs associated Ca^{2+} responses aligned to the peak of the EPSPs (average of five to nine responses). The 3D scanning trajectories cover the majority of the dendritic arbor, and the segments were imaged simultaneously in different combinations (Figure S1) in the apical (top) and basal (bottom) regions. Numbered arrows correspond to segments in (A) and point distally. Asterisks indicate small compartmentalized synaptic responses.

(C) Average SPW-EPSP-induced (red), SPW-AP-induced (green, with 1 AP), and backpropagating AP-induced (black, 5 APs) 3D Ca^{2+} responses as a function of distance from the soma. Mean ± SEM, n = 5 cells. Back-propagating APs were induced between SPW events. Note the complementary distribution of the red and green versus black graphs.

(D) Average apical and basal dendritic Ca^{2+} signals during SPW-EPSPs (mean ± SEM, n = 5 cells).

See also Figure S1, Table S1, and Movies S1, S2, S3, and S4.

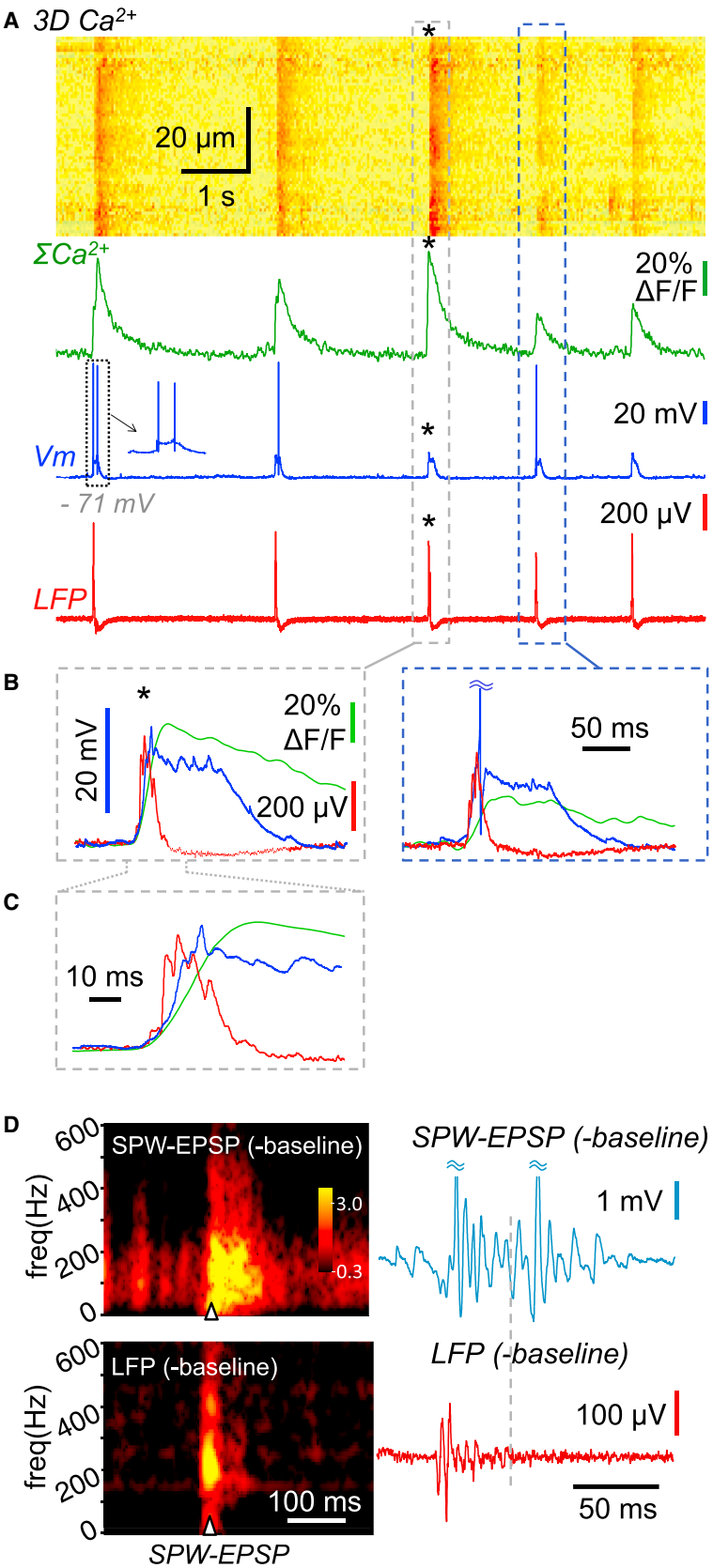

Figure 2. SPW-Associated Dendritic Spikes and Interneuronal Ripple Oscillation

(A) Representative 3D Ca^{2+} response (top) recorded during five successive SPW-R events in a single, long dendritic segment shows that Ca^{2+} signals invade the full apical dendritic segment both in the presence and absence (asterisks) of somatic APs. The spatially integrated dendritic Ca^{2+} response (green) is shown with the simultaneously recorded somatic membrane (blue) and CA1 local field potentials (red, str. pyramidale).

(B) Overlaid Ca^{2+} (green), LFP (red), and whole-cell membrane potential (blue) traces from the two boxed areas in (A).

(C) Traces in (B) shown at a higher magnification.

(D) Left: averaged spectrograms of baseline-subtracted SPW-EPSPs and LFPs (n = 7). Right: representative individual traces after baseline subtraction are shown on the same timescale. See also Figure S2.

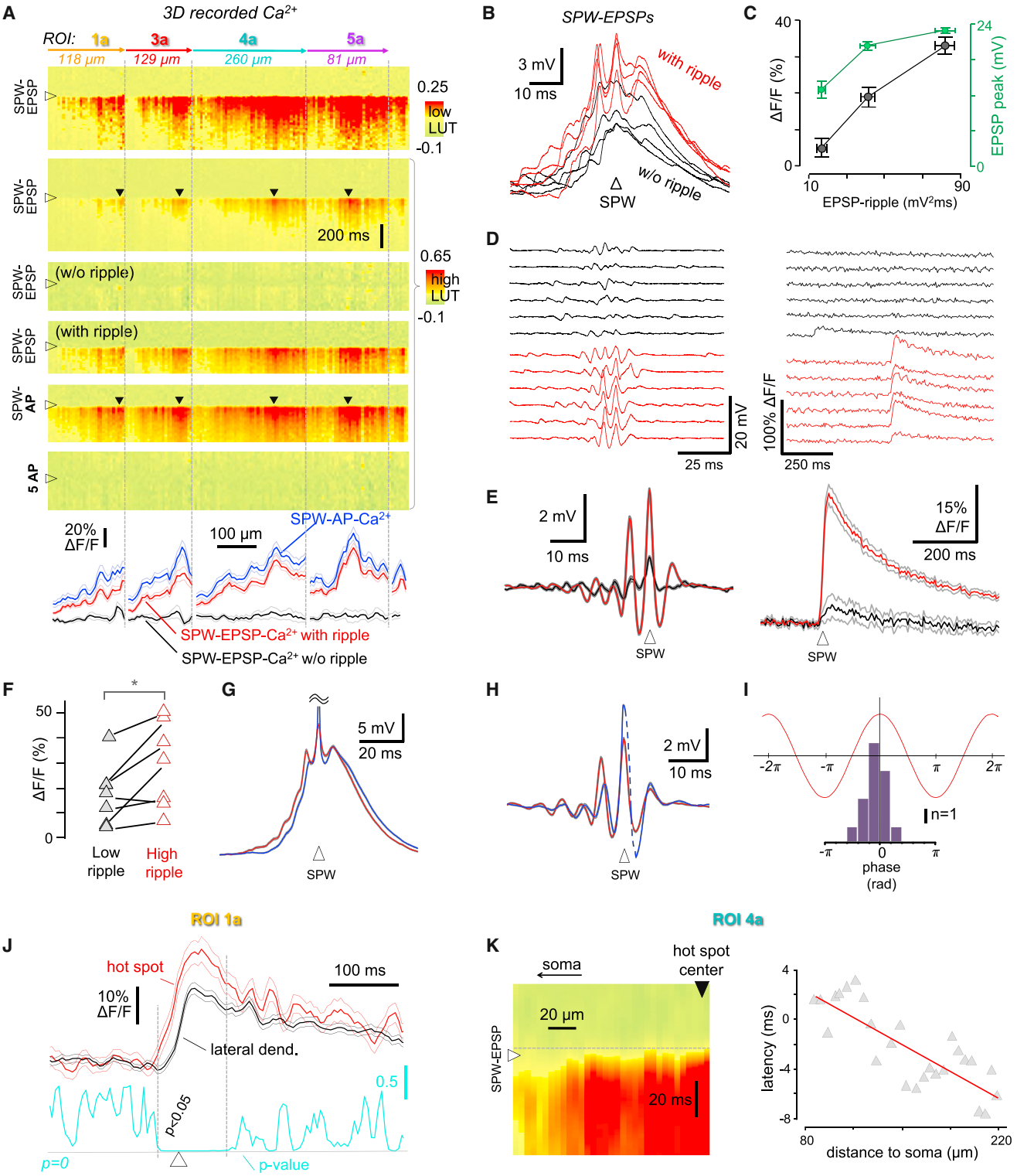

Figure 3. Dendritic Spikes Are Associated with Interneuronal Ripple Oscillations and Initiated in Multiple Hot Spots during SPW-Rs

(A) Top: average SPW-EPSP-, SPW-AP-, and bAP-associated 3D Ca^{2+} responses, recorded simultaneously in the apical dendritic segments in Figure 1A. The look-up table with high ΔF/F values (high LUT) revealed hot spots (black triangles). The subgroup of SPW-EPSPs with interneuronal ripple oscillations (with ripple) induced larger 3D Ca^{2+} responses than those without oscillations (w/o ripple). In these distant dendritic locations, five bAPs (5 bAP) did not induce any response. Bottom: spatial distribution of peak 3D Ca^{2+} responses (mean ± SEM).

(legend continued on next page)

as propagating dendritic Ca^{2+} spikes, could occur. In order to test this hypothesis, we established a set of criteria based on previous definitions (Katona et al., 2011; Losonczy and Magee, 2006; Stuart et al., 1999), the fulfillment of which strongly indicate that there is a dynamic switch in integration mode and that dendritic spikes are generated in FS-PV INs during SPW-Rs: (1) spikes are detectable in the membrane potential signal, (2) spike initiation is dendritic in origin, (3) spikes actively propagate into neighboring dendritic segments, (4) spikes are initiated in an all-or-nothing manner above a well-defined threshold, and (5) spikes are mediated by voltage-gated ion channels. We address these criteria in detail in the following sections.

Interneuronal Ripple Oscillations Are Associated with the Dendritic Spikes

The first criterion was addressed by studying the somatic membrane potential in relation to simultaneously recorded 3D Ca^{2+} responses. On average, the amplitude of the dendritic 3D Ca^{2+} responses correlated positively with the amplitude of the EPSPs ($r = 0.84$) (Figures S3E and S3F) and with the number of APs in the suprathreshold case (Figure S3E). However, we noticed a large event-to-event variability in the amplitude of the dendritic Ca^{2+} signals (Figure 2); specifically, SPW-EPSPs with long oscillating plateau-potentials were occasionally accompanied by Ca^{2+} events larger than those of SPW-APs (Figure 2). This oscillation-like behavior of the somatic membrane potential was captured by our baseline subtraction method (Experimental Procedures; Figure S2) and with short-time Fourier transforms (spectrograms) of the somatic membrane potential (Figures 2D and S2D). The oscillation frequency of SPW-EPSPs increased rapidly before the SPW-EPSP peak, had a maximum at the peak (f_{max} 270.3 ± 18.18 Hz, n = 11), then decreased at a slower rate below 239.97 ± 19.25 Hz, while its duration extended 17.1 ± 3.19 ms beyond the termination of the network LFP signal (LFP_{FWHM} 12.23 ± 1.85 ms, $EPSP_{FWHM}$ 29.37 ± 2.49 ms, $p = 0.0001$) (Figures 2B–2D and S2D). These data provide evidence that individual neurons can generate additional membrane oscillations in the ripple frequency range (defined as interneuronal ripple oscillations) after network oscillations have terminated. Moreover, in over 50% of the cells, we simultaneously recorded individual SPW-EPSPs and LFP traces whose phases, frequencies, and amplitudes did not correlate, despite the fact that the average SPW-EPSP and LFP signals correlated well (Figure S2E). These data also suggested that intrinsic membrane mechanisms may contribute to the generation of the dendritic Ca^{2+} spikes and accompanying interneuronal ripple oscillations; therefore, we further investigated the relationship between the oscillations and Ca^{2+} responses.

The amplitude of SPW-EPSP-associated Ca^{2+} responses correlated well with the power of interneuronal ripple oscillations in individual dendritic segments and also in spatial averages across dendrites (Figures 3A–3F and S3E–S3J, r = 0.59). Although this correlation appeared in the form of a continuous distribution (Figure S3G), a subgroup of SPW-EPSPs with no interneuronal ripple oscillations and with small Ca^{2+} amplitudes could be separated out with cluster analysis (Figure S3J). This nonoscillating subgroup of SPW-EPSPs was not associated with large Ca^{2+} responses invading whole dendritic segments (Figures 3A–3D). Baseline-corrected and peak-aligned SPW-EPSPs and SPW-APs showed interneuronal ripple oscillations with similar frequencies and phase values (239.97 ± 18.35 Hz and 239.70 ± 11.00 Hz, respectively, $p > 0.3$, n = 10) (Figures 3G and 3H). Moreover, the AP output of FS-PV INs was tightly phase-locked to these interneuronal ripple oscillations (Figure 3I). This also means that the dendritic spikes induced by synchronized network activity can transiently switch the input-output transformation function of FS-PV INs from the well-characterized submillisecond precision of EPSP-AP coupling to a slower integration scale, where interneuron output is gated in phase synchrony with interneuronal ripple oscillations.

Initiation and Propagation of the SPW-R-Associated Dendritic Spikes from Hot Spots

We used high-speed 3D trajectory scanning to define the dendritic origin of the putative Ca^{2+} spikes referred to in the second criterion. Long apical segments were examined in the distal dendritic zone (up to 308 μm from the soma), where the amplitude of 3D Ca^{2+} responses induced by five bAPs was below the detection threshold (Figure 3A). As shown above, large 3D Ca^{2+} responses associated with either SPW-EPSPs or SPW-APs effectively invaded these apical dendritic segments and formed simultaneous local maxima, i.e., hot spots, in several segments (Figure 3A). The relevance of hot spots is further supported by the fact that, although the occurrence of APs boosted the dendritic 3D Ca^{2+} response in the measured distal segments evenly

(B) Representative SPW-EPSPs with (red) and without (black) interneuronal ripple oscillations.
(C) Average dendritic Ca^{2+} transients (black) and simultaneously recorded EPSPs (green) as a function of the power of interneuronal ripple oscillations (mean ± SEM).
(D) Left: individual SPW-EPSPs after baseline subtraction with (red) and without (black) oscillations. Right: corresponding dendritic Ca^{2+} transients, averaged in regions of interest (ROIs) shown in (A).
(E) Left: peak-aligned oscillating (red) and nonoscillating (black) SPW-EPSPs after baseline subtraction (mean ± SEM, n = 30). Right: corresponding mean dendritic Ca^{2+} transients averaged in the regions shown in (A).
(F) Mean dendritic Ca^{2+} transients associated with SPW-EPSPs with high (red) and low (black) interneuronal ripple oscillations (n = 7 cells).
(G) Average SPW-APs (blue) and SPW-EPSPs (red) showing similar interneuronal ripple oscillations. (mean ± SEM, n = 30).
(H) The same as (G) after baseline subtraction.
(I) Binned firing probability relative to the phase of the interneuronal ripple oscillations (n = 17 cells).
(J) The Ca^{2+} signal in the center of the hot spot (red) in dendritic segment 1a in (A) was larger and significantly (cyan) preceded the Ca^{2+} signal of adjacent dendritic regions (black) in the rising phase (mean ± SEM).
(K) Left: propagation of the SPW-EPSP-associated Ca^{2+} spike from the center of the hot spot of region 4a toward the soma. Right: corresponding Ca^{2+} signal onset latency times. Red line is a linear fit (r = 0.65).
See also Figure S3.

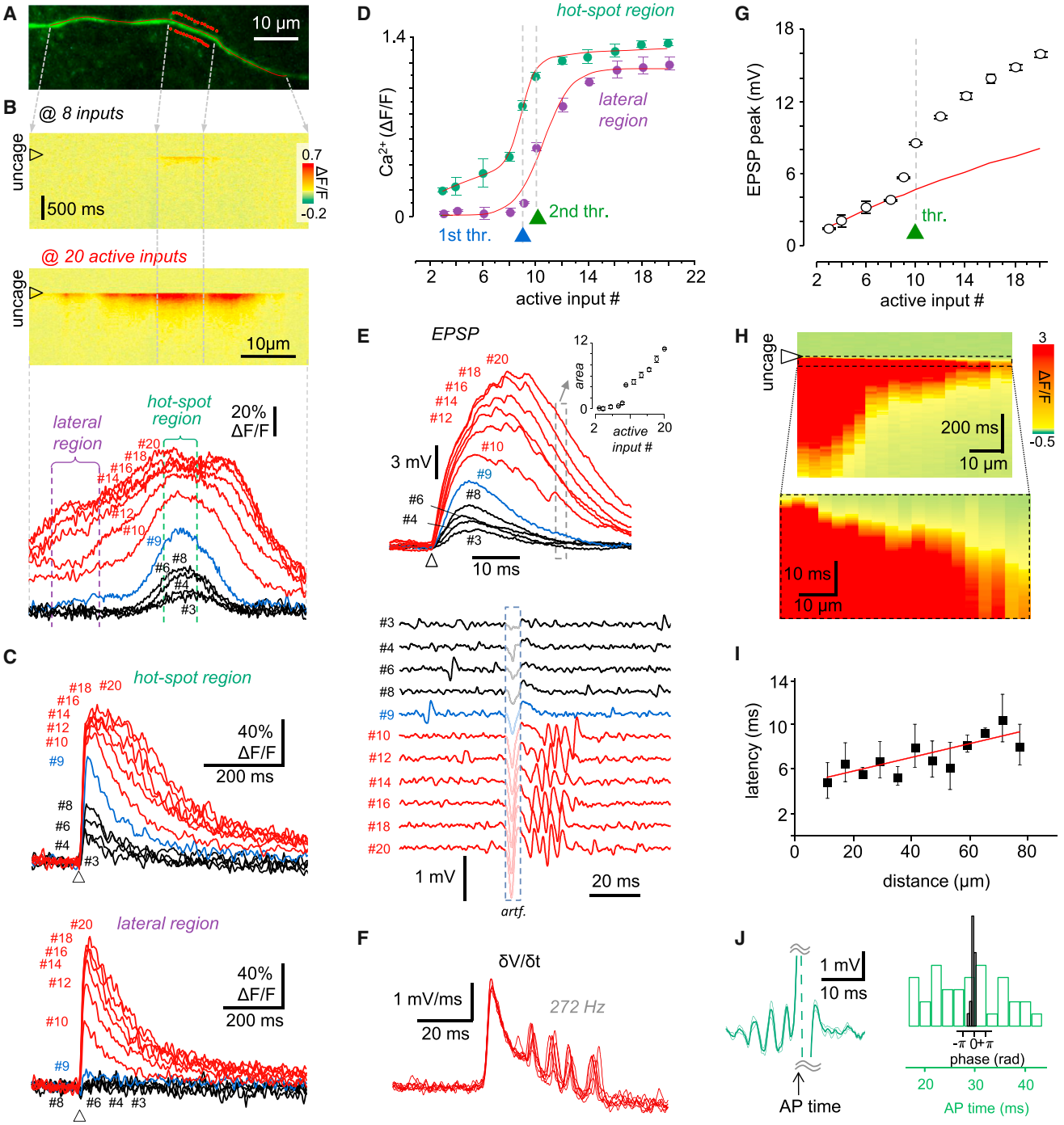

Figure 4. Synchronous Activation of Clustered Glutamatergic Inputs Reproduces SPW-R-Associated Dendritic Ca^{2+} Spikes and Related Interneuronal Ripple Oscillations

(A) Maximum intensity z projection image of a dendritic segment of an FS-PV IN. Red points are active input locations used for patterned two-photon glutamate uncaging in the presence of DNI-Glu•TFA.

(B–G) Uncaging-evoked Ca^{2+} responses measured along the red line in (A) and the corresponding somatically subthreshold EPSPs below the first threshold (black), at the first threshold (blue), and above the second threshold (red). (B) Average Ca^{2+} responses (n = 5) induced by uncaging with a just-subthreshold number of active inputs (top) and at a suprathreshold number of active inputs (middle). Bottom: spatial distribution of the peak Ca^{2+} responses at an increasing number of active inputs. (C) Ca^{2+} transients derived at the hot spot (top) and at the lateral dendritic (bottom) regions in (B) at an increasing number of active inputs. (D) Mean peak Ca^{2+} responses (n = 4 measurements). Boltzmann fits are shown in red. Note the sharp increase at the first and second thresholds in the hot spot and lateral dendritic regions, respectively (mean ± SEM). (E) Corresponding individual EPSPs with (bottom) and without (top) baseline subtraction demonstrate

(legend continued on next page)

by 41.3% ± 2.9% (n = 5 cells over 150 μm distance) (Figure 3A, see also Figure 1B), the location of hot spots also remained well-preserved in this suprathreshold case (Figure 3A).

Next, we wanted to demonstrate the active propagation of the putative spikes from their dendritic initiation sites to the adjacent dendritic segments (third criterion) by applying our previously developed temporal super-resolution method (Katona et al., 2012). We first selected only the subthreshold SPW-EPSPs for analysis, in order to avoid the putative effect of interactions between dendritic spike and AP generation. As the SPW-EPSP-associated 3D Ca^{2+} responses typically showed simultaneous hot spots in more than one dendritic location (Figure 3A), we selectively measured fast propagation from these multiple hot spots to neighboring dendritic segments. The 3D Ca^{2+} responses were not only larger in the hot spots (333% ± 51%, n = 17 regions in n = 9 cells), but they also preceded the Ca^{2+} signals in the adjacent dendritic segments (41.5 ± 12.7 μm from the center of the hot spot, Figure 3J) by 12.8 ± 2.4 ms, indicating that hot spots are the initiation sites of the dendritic spike. Supporting the regenerative nature of the dendritic spikes, the propagation speed from the hot spots toward lateral dendritic segments could be clearly measured in 68.8% ± 8.2% of long dendritic segments (222.1 ± 63.0 μm, n = 13) (Figure 3K), yielding an average propagation speed of 34.22 ± 4.32 μm/ms, a substantially higher speed than that expected from diffusion (Goldberg et al., 2003a; Katona et al., 2011). SPW-EPSP-associated Ca^{2+} spikes that approximated the somatic region propagated only in the direction of the soma, and never from the soma to dendrites, suggesting their origin is dendritic. These data indicate that the SPW-R-associated and broadly distributed Ca^{2+} signals demonstrated above are regenerative dendritic events with active propagation from dendritic hot spots.

Spatially and Temporally Clustered Inputs Generate the Dendritic Spikes

In order to find the minimum number of clustered excitatory inputs that are needed to evoke the regenerative event in an all-or-nothing manner (fourth criterion), we simulated active excitatory synaptic inputs by using two-photon glutamate uncaging in temporally and spatially clustered patterns (Katona et al., 2011). To model the buildup of large-amplitude SPW-EPSPs (29.37 ± 2.49 ms, 22.6 ± 1.63 mV, n = 12, see Figures 2B and 3B) from small unitary inputs (<1 mV) (Ali et al., 1998), tens of unitary inputs needed to be activated in a short time window. However, the quantum efficiency of the widely used MNI-glutamate was not high enough to repetitively activate such a high number of clustered inputs within the time window of ripple oscillations (5–6 ms) without causing photodamage in consecutive measurements. Therefore, we developed a caged glutamate compound, DNI-glutamate•TFA (DNI-Glu•TFA), which has a 7.17 ± 0.84 times higher two-photon uncaging efficiency than MNI-glutamate (see Supplemental Information).

In contrast to the expected linear or sublinear dendritic input-output transformation demonstrated earlier in FS-PV INs (Hu et al., 2010; Nörenberg et al., 2010) and two types of cerebellar interneurons (Abrahamsson et al., 2012; Vervaeke et al., 2012), the uncaging-evoked Ca^{2+} signal in the hot spot region showed a step-like nonlinear increase (Figures 4A–4D) at a given active input number, defined as the first threshold (11.04 ± 1.4 active inputs, n = 9 cells, see Experimental Procedures), followed by a more modest increase at a slower rate at a progressively increasing active input number (Equations S3 and S4 in the Supplemental Experimental Procedures). The uncaging-evoked Ca^{2+} signal reproduced well the spontaneous SPW-R-associated responses from the hot spots. Interestingly, the first threshold was followed by a separate second threshold (Figure 4D) that was clearly visible outside the input zone (termed lateral dendritic region) (Figures 4B–4D and S4A–S4E) where the uncaging-evoked Ca^{2+} signal showed a sigmoid-like increase, at 30.3 ± 4.0 active excitatory inputs (range 10–47, n = 9 cells). As the average release probability of excitatory synapses onto FS-PV INs is 0.75 ± 0.19 (Gulyás et al., 1993), the first and second threshold of active input number correspond to the activation of ~15 and ~40 release sites, respectively. The simultaneously recorded somatic membrane potential remained below the AP threshold (Figures 4E and S4A). Moreover, the spatial distribution of the Ca^{2+} increase in the lateral dendritic regions showed a "plateau-like" characteristic above the second threshold (see control responses in Figures 5B and S5 for the plateau-like increase of Ca^{2+} in the lateral dendritic regions). Although the amplitude of Ca^{2+} plateaus slightly decreased as a function of distance from the border of the hot spot region, it reproduced the large, propagating Ca^{2+} waves generated near hot spots during spontaneous SPW-EPSPs (Figure 3). If the uncaging-evoked Ca^{2+} plateau in the lateral dendritic region does also represent a regenerative spike, there should also be active propagation (third criterion). Indeed, we were able to measure a propagation speed of 17.4 ± 3.6 μm/ms (Figures 4H and 4I) in 85.1 ± 16.4 μm-long dendritic segments (n = 5 cells), which is similar to the propagation speed of the large, spontaneous SPW-EPSP-associated dendritic 3D Ca^{2+} responses. The small difference in the propagation speed between spontaneous SPW-EPSP-associated Ca^{2+} responses (Figure 3K) and uncaging-evoked Ca^{2+} signals could be explained by the lack of activated synaptic inputs in the lateral dendritic regions upon uncaging, which may decrease the local voltage. Indeed, Ca^{2+}

that ripple oscillations appear. Inset shows EPSP integrals calculated from data in the boxed region (mean ± SEM). (F) First derivative of representative EPSPs induced by 32 active inputs shows the stability of the oscillations. (G) Amplitude of the simultaneously recorded EPSP peak versus the number of active inputs (mean ± SEM). Dashed line and triangle indicate threshold input number (thr.). Initial part of the input-output curve was fitted by using Equation S3 in the Supplemental Experimental Procedures (red).

(H) Propagation of the uncaging-evoked dendritic spike from the border of a hot spot region in the lateral direction.

(I) Corresponding Ca^{2+} signal onset latency times. Linear fits are shown in red.

(J) Left: suprathreshold voltage responses (mean ± SEM) induced by 59 active inputs, baseline-subtracted and aligned to the peak of the AP. Right: histogram of AP timing relative to the phase of interneuronal ripple oscillation (gray, n = 18) and relative to the EPSP onset time (green, n = 36). The two x axes were overlaid according to the average oscillation time.

See also Figure S4.

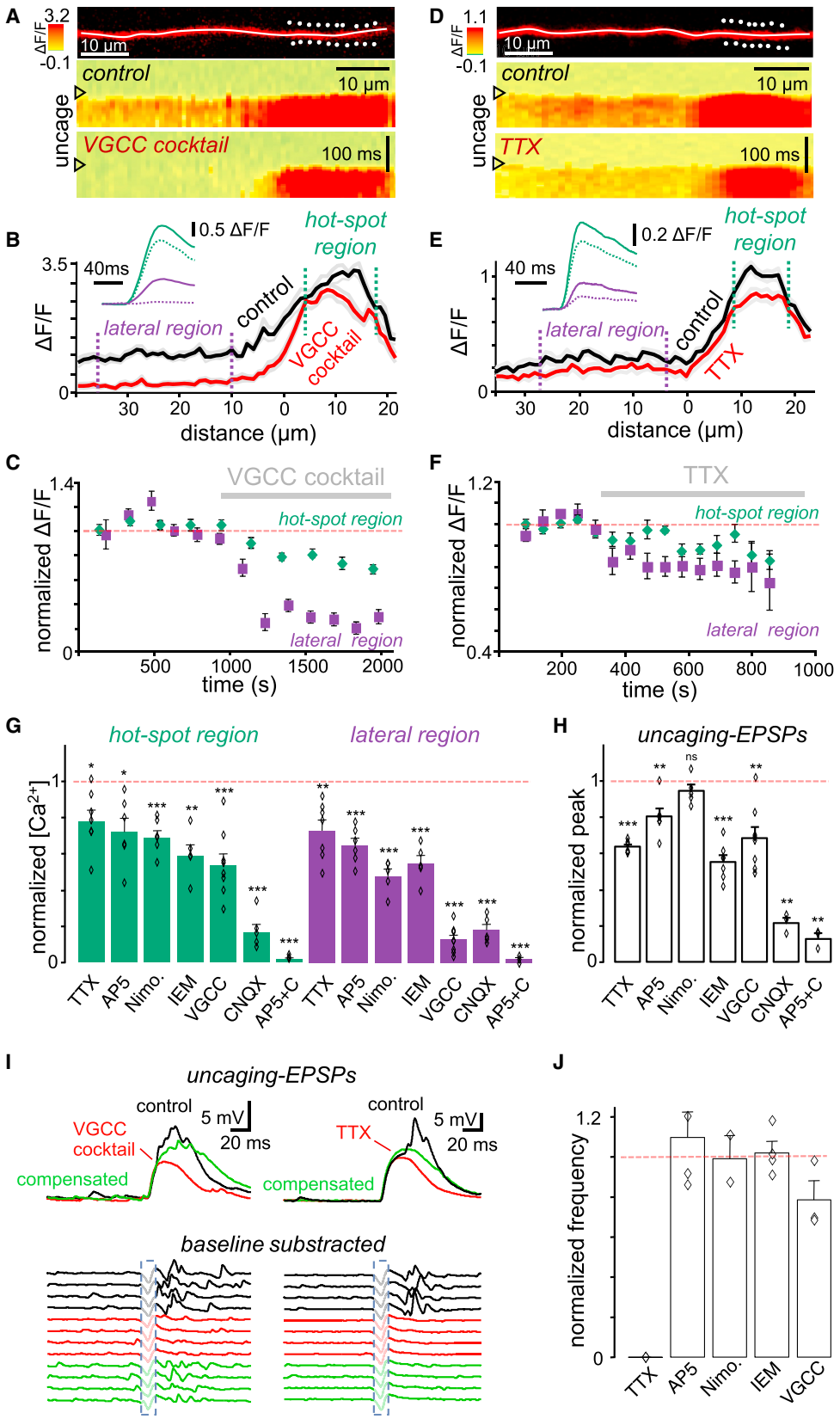

(legend on next page)

responses were larger when the activated inputs were more widely distributed along the dendrite (Figures S4I–S4K). These data are in good agreement with the increase in the amplitude of backpropagating AP-associated Ca^{2+} responses during SPW-Rs (Figure 1C), when many synchronous dendritic inputs arrive.

Short Dendritic Segments Generate Oscillations with Ripple Frequency

To establish how the uncaging-induced Ca^{2+} spikes were reflected in the simultaneously recorded somatic membrane potential (first criterion), we first investigated the input-output characteristic of FS-PV INs. The initial linear (Figures 4E and 4G) or sublinear (Figures S4A–S4E) increase in the amplitude of somatic EPSPs was followed by a step-like increase at the second threshold number of active inputs, and the amplitude progressively increased thereafter as a function of increasing number of active inputs at a slower rate above the second threshold (Figures 4E, 4G, and S4A–S4E; Equations S3 and S4 in the Supplemental Experimental Procedures). When the second threshold input number was higher (above ~15 active inputs), an initially sublinear increase in the input-output function (instead of a linear increase) was revealed, which fitted well to Equation S3 in the Supplemental Experimental Procedures, on which a sigmoid-like increase (well fitted to Equation S4 in the Supplemental Experimental Procedures) was superimposed at the second threshold number of active inputs (Figures S4A and S4B). A similar sublinear integration rule of EPSPs, but without the step-like increase, has also been demonstrated in other interneurons in silent acute slices (Abrahamsson et al., 2012; Vervaeke et al., 2012). The sigmoid-like increase in EPSP amplitude was similar to the previous low threshold case and was also combined with a simultaneously occurring Ca^{2+} increase in the input and lateral dendritic regions (Figures S4C–S4E).

Somatic interneuronal ripple oscillations above the second threshold could be detected in 17 out of 35 cells (48.57%). In 11 cells, the evoked oscillation was robust and stable, and its frequency (219.3 ± 14.5 Hz) closely approximated the interneuronal ripple oscillation frequency of spontaneous SPW-EPSPs (239.97 ± 18.35 Hz) (Figure 4E). To show more directly that the appearance of interneuronal ripple oscillations, and not only the increased EPSP amplitude, is responsible for the nonlinear Ca^{2+} increase, we investigated the relationship between the uncaging-evoked EPSPs and the membrane potential oscillation. We found that EPSPs with initially overlapping time curves induced 41.8% ± 9.6% larger dendritic Ca^{2+} responses when interneuronal ripple oscillations were riding on them ($p = 0.008$; $n = 6$ cells) (Figures S4F–S4H). When the active input number was increased progressively, the evoked oscillation onset latency became shorter, and interneuronal ripple oscillations varied less in amplitude and phase; nevertheless, the frequency of the evoked interneuronal ripple oscillations did not change ($p > 0.38$, t test) (Figure 4F and see also Figure S4I, which shows additional data for 32 active inputs). When spatially distributed activation patterns were used instead of clustered ones, the frequency of the evoked interneuronal ripple oscillations was similar ($p = 0.23$, t test, $n = 7$) (Figures S4I and S4J). However, distributed input patterns induced ripple oscillations in more dendritic segments (73.68%, 14/19 segments in 14/19 cells) and produced more oscillation cycles upon each induction (Figures S4I and S4J).

Finally, we investigated the functional relevance of interneuronal ripple oscillations. We observed that the distribution of somatic APs relative to EPSP onset time was rather broad in the presence of interneuronal ripple oscillations. By contrast, APs were strongly coupled to the peaks of the oscillation (Figures 4J and S4L): this agrees with our data from spontaneous SPW-Rs (Figure 3I). We concluded that the well-known fast, reliable EPSP-AP coupling of FS-PV INs is replaced during periods of strong excitation by an integration mode where the timing of AP output is determined primarily by the phase of interneuronal ripple oscillations.

Spikes Are Mediated by L-type Ca^{2+} Channels and Ripples by Na^{+} Channels

In order to investigate the functional role of different ion channels in the mechanism underlying dendritic ripples and spikes (fifth criterion), we activated spatiotemporally clustered patterns that were above the second threshold, but below the threshold for somatic AP generation (43.8 ± 2.9 active inputs). Long dendritic segments (Figures 5A, 5D, and S5) were selected, and inputs were activated at only one end of the imaged (Fluo4 and Alexa594) dendritic segments in order to better separate the

Figure 5. Dendritic Ca^{2+} Spikes Are Mediated Predominantly by L-type Ca^{2+} Channels and the Related Interneuronal Ripple Oscillations Are Generated by Na^{+} Channels

(A–C) Effect of VGCC blockers on uncaging-evoked Ca^{2+} responses. (A) Maximum intensity z projection image of a distal dendritic segment of an FS-PV IN. Average uncaging-evoked Ca^{2+} responses in control conditions (middle) and in the presence of a cocktail of VGCC blockers (bottom). White points are active input locations used for DNI-Glu•TFA uncaging (top). (B) Spatial distribution of the peak dendritic Ca^{2+} response (mean ± SEM, n = 13/10 control/VGCC) measured along the white line in (A) under control conditions (black) and in the presence of VGCC blockers (red). Inset: mean Ca^{2+} transients derived from the hot spot (green) and lateral dendritic (magenta) regions before (solid line) and after (dashed line) application of the VGCC cocktail. (C) Time course of the effect of the VGCC cocktail on Ca^{2+} responses in the hot spot (green) and lateral dendritic (magenta) regions (mean ± SEM, n = 5 cells).

(D–F) The same as (A–C), respectively, but for TTX (mean ± SEM, n = 6/10 control/TTX and n = 7 cells).

(G) Effect of different ion channel blockers on the peak amplitude of $[Ca^{2+}]$. Nimo. and AP5+C indicate nimodipine and AP5+CNQX, respectively (mean ± SEM, rhomboids indicate individual neurons).

(H) The same as (G), but for simultaneously recorded EPSPs.

(I) Subthreshold EPSPs showing interneuronal ripple oscillations with (bottom) and without (top) baseline subtraction in control conditions (black), but not in the presence of TTX or the VGCC cocktail (red traces left and right respectively). When the uncaging laser intensity was increased (compensated), interneuronal ripple oscillations were restored in the presence of VGCC blockers, but not when TTX was present.

(J) The effect of ion-channel blockers on interneuronal ripple oscillations (mean ± SEM, rhomboids indicate individual neurons). Ripple oscillations were only abolished by TTX.

See also Figure S5.

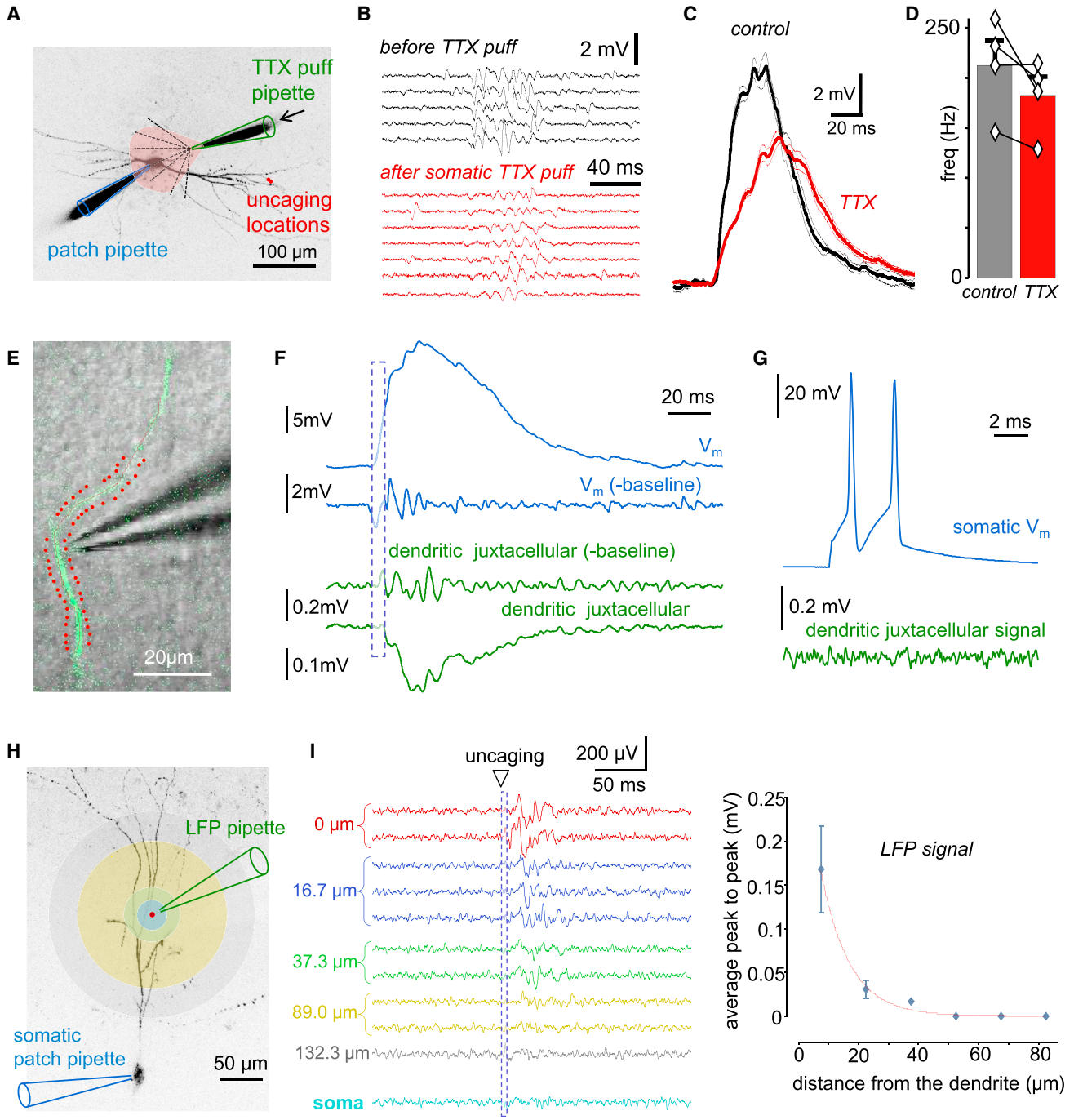

Figure 6. Interneuronal Ripple Oscillations Can Be Detected by Juxtacellular Recording and Are Preserved following Somatic TTX Injection

(A) An inverted image of an FS-PV IN with the somatic recording and local TTX injection pipettes.

(B) Representative somatic EPSPs after baseline subtraction show interneuronal ripple oscillations in control conditions (black) and after local TTX injection (red). Oscillations were induced by using spatiotemporally clustered input patterns in the distal dendritic location indicated in (A).

(C) Average of the EPSPs (mean ± SEM).

(D) Oscillation frequencies in the control case and after local TTX injection were not significantly different (mean ± SEM, n = 4 cells).

(E) Overlaid transmitted gradient and two-photon images of a dendritic segment from an FS-PV IN.

(F) The juxtacellular signal (green) from the dendritic location in (E), and the simultaneously recorded somatic membrane potential (blue) are shown with and without baseline substraction. Interneuronal ripple oscillations were induced by uncaging at the red points in (E).

(G) Somatically evoked bAPs were below the detection threshold in the juxtacellular signal (green) in the dendritic location in (E).

(legend continued on next page)

central and lateral dendritic regions in the pharmacological experiments. For a precise quantification of the pharmacological effects, we had to take into account the saturation and nonlinear response of the Ca^{2+} dye, and we therefore transformed the relative fluorescence data into [Ca^{2+}] using Equation S5 in the Supplemental Experimental Procedures.

AMPA and NMDA receptors play a dominant role in triggering dendritic Ca^{2+} response: the combined application of AMPA and NMDA receptor blockers (CNQX and AP5, respectively) reduced the Ca^{2+} responses to almost zero (Figure 5G) in both regions. In the lateral dendritic region, VGCC blockers evoked a drastic reduction in the Ca^{2+} signal (Figures 5A–5C, 5G, and S5J). Therefore, our data indicate that VGCCs are mainly responsible for the Ca^{2+} influx in the lateral dendritic region and are thus responsible for the dendritic Ca^{2+} spike. Hippocampal interneurons express P/Q-, R-, L-, N-, and T-type VGCCs (Vinet and Sík, 2006), but we found that the L-type VGCC blocker nimodipine had the greatest effect on the Ca^{2+} responses of FS-PV INs, both in the present study and in our earlier work (Chiovini et al., 2010). In the central hot spot region, the source of Ca^{2+} influx was more complex as it was simultaneously mediated by NMDA, calcium-permeable AMPA receptors and VGCCs, and further amplified by Na^+ channels (Figures 5 and S5). In line with other observations, we noted that Ca^{2+}-permeable AMPA receptors had a larger effect on the postsynaptic Ca^{2+} influx than NMDA receptors (Goldberg et al., 2003a, 2003c; Goldberg and Yuste, 2005; Lamsa et al., 2007; Topolnik, 2012). The amplitude and area of the simultaneously recorded uncaging-evoked EPSPs was significantly decreased by all the ion-channel blockers we tested (Figures 5H, 5I, and S5K). This change in the somatic EPSP likely reflects a similar change in the local dendritic voltage response, which may by itself affect the generation of membrane ripple oscillations. To test this possibility, we compensated for the EPSP amplitude drop by increasing the uncaging laser intensity when oscillations disappeared until the amplitude of the uncaging-evoked EPSPs reached the control value again, or interneuronal ripple oscillations reappeared. Under these circumstances, the oscillations recovered (or remained stable) for all pharmacons except during TTX application, which completely eliminated interneuronal ripple oscillations, indicating that they are dependent on Na^+ channel activation (Figures 5I, 5J, and S5). In contrast, the oscillation frequency did not change significantly in the presence of AP5, nimodipine, IEM-1460, or the cocktail of VGCC blockers (Figure 5J). Our results show that the propagating dendritic Ca^{2+} spikes are predominantly mediated by L-type Ca^{2+} channels, while the related interneuronal ripple oscillations are determined by voltage-gated Na^+ channels. In summary, we can conclude that dendritic spikes exist in FS-PV INs, as the observed events satisfied all five of the criteria defined initially.

To further validate the dendritic origin of interneuronal ripple oscillations, we locally injected TTX (10 μM) onto the axosomatic region (Figure 6A). The local TTX application eliminated all APs induced by somatic current injection (Figure S6H), but it did not block interneuronal ripple oscillations (control 212.83 ± 24.18 Hz; TTX puff 182.72 ± 18.72 Hz, paired t test, p = 0.156) (Figures 6B–6D). This confirms their dendritic origin. In order to detect local membrane potential oscillations more directly, in a different set of experiments we combined whole-cell recordings with two-photon guided dendritic juxtacellular recordings (Figures 6E–6G) at distal dendritic locations (266.37 ± 67.05 μm, mean ± SD). Oscillations were induced by using spatiotemporally clustered input patterns, as above. Interneuronal ripple oscillations could be simultaneously detected in the somatic membrane potential and in juxtacellular signals (Figure 6F) at distal dendritic locations, where the bAP-induced juxtacellular signal was below the detection threshold (Figure 6G). The oscillation amplitude in the LFP signal decreased as the dendritic recording pipette was gradually moved away from the activated dendritic segment, but remained high enough to be detected at distances up to ~40 μm (Figures 6H–6I, spatial decay constant 15.6 ± 4.9 μm, n = 4). Finally, we showed that, in contrast to somatic AP, the threshold of interneuronal ripple oscillations changed in proportion to the somatic membrane potential (Figures S6A–S6G), which reflects the weak control over the oscillations by the somatic membrane potential. These data, together with the local uncaging experiments and propagation measurements, strongly support the dendritic origin of the interneuronal ripple oscillations.

Modeling of Dendritic Spikes in FS-PV INs

Our experimental results suggest that dendritic voltage-gated Ca^{2+} and Na^+ channels may be primarily responsible for the supralinear responses and the accompanying fast interneuronal ripple oscillations. We further investigated the feasibility of this scenario by constructing a detailed compartmental model of a CA1 basket cell, based on a morphological reconstruction (Figures 7A and S7; Supplemental Experimental Procedures). We found that a neuronal model that contained an elevated density of voltage-gated Na^+ channels and high-voltage-activated, slowly inactivating Ca^{2+} channels in distal dendritic segments (but lower densities of these channels in more proximal dendrites [Hu et al., 2010]) could faithfully capture several key experimental observations. Simulated excitatory synaptic input to middle and distal apical dendritic branches evoked brief local EPSPs, and corresponding small somatic EPSPs, when the activated synaptic conductance was low. As synaptic conductance was gradually increased, the response initially increased in a slightly sublinear fashion and then, upon reaching a threshold, a more sustained dendritic plateau potential appeared, accompanied by fast dendritic spikes (Figure 7B). Analysis of membrane currents in the model suggested that the slow spike was mediated mainly by dendritic voltage-gated Ca^{2+} channels, while the fast spikes were generated by dendritic voltage-gated Na^+ and K^+ channels (Figure 7D). The dendritic spikes were observable at the soma as a sudden increase in EPSP amplitude and duration

(H) The second patch pipette was used to record the LFP signal at variable distances from the dendrite. The same inputs, in the same dendritic region, were activated as shown in (E) to induce interneuronal ripple oscillations.
(I) Individual LFP signals and amplitude of the oscillations (mean ± SEM, n = 4) as a function of distance from the activated interneuronal dendritic segment. Red line is an exponential fit.
See also Figure S6.

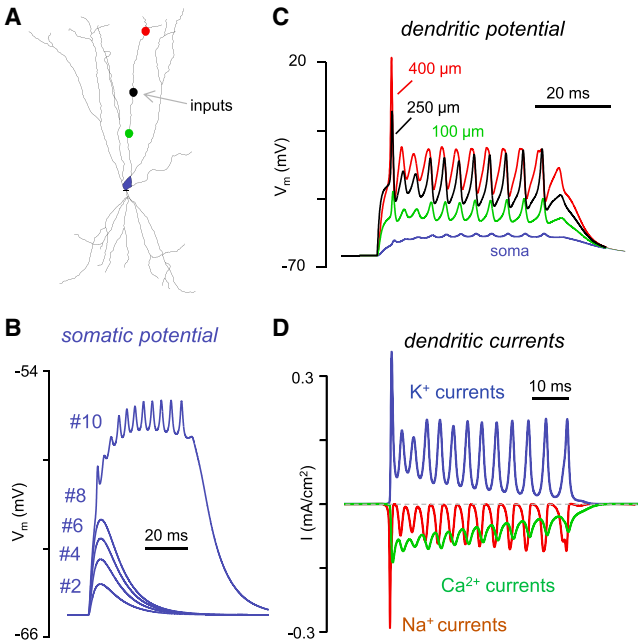

Figure 7. Modeling of Dendritic Spikes in FS-PV INs

(A) Morphology of the fast-spiking CA1 basket cell used in the simulations. Black point indicates location of excitatory inputs.

(B) Responses at the soma to an increasing number of excitatory synaptic inputs to the location marked in (A).

(C) Responses to ten active inputs at three different dendritic locations, indicated in (A) and at the soma (blue).

(D) Corresponding ion currents through voltage-gated K^+, Na^+, and Ca^{2+} channels at the red point in (A). Note that the Ca^{2+} and K^+ currents follow the Na^+ current during the oscillations.

See also Figure S7.

and a fast (ripple-frequency) oscillation riding on top of the slower depolarizing component (Figure 7C). Thus, our modeling results confirm that dendritic spikes evoked in FS-PV INs by strong excitatory synaptic input provide an explanation for our experimental observations (Table S2).

DISCUSSION

A Dynamic Switch in the Mode of Dendritic Integration in FS-PV INs during SPW-Rs

Our results paint a far more active and dynamic picture of FS-PV IN dendrites than the currently prevailing view. Although the presence of Ca^{2+}-permeable AMPA and NMDA receptors, as well as voltage-gated Na^+, Ca^{2+}, and K^+ channels in FS-PV IN dendrites had been demonstrated in earlier studies, it has been proposed that the fast electrical and Ca^{2+} signals provided by these channels are spatially and temporally attenuated and well-compartmentalized (Goldberg and Yuste, 2005; Goldberg et al., 2003c; Hu et al., 2010). Such functional dampening and spatial segregation are thought to endow these interneurons with prompt and effective signal integration in the sublinear range. Our results, based on a caged-glutamate compound and 3D imaging methods, challenge this classical view of the functional role of interneurons by demonstrating a network-activity-dependent dynamic switch in dendritic integration mode. We have shown that passive, well-dampened FS-PV IN dendrites can be transiently activated by a high number of spatially and temporally coincident excitatory inputs during SPW-Rs. In this active state, several physiological properties of FS-PV INs are changed (Table S2): (1) AP-associated Ca^{2+} responses are not compartmentalized to the proximal dendritic regions but also invade distal dendritic segments, (2) dendritic spikes occur, in contrast to the low-activity baseline state (Hu et al., 2010), (3) supralinear dendritic integration with a dual-integration threshold replaces linear or sublinear summation, (4) compartmentalized synaptic Ca^{2+} signals are replaced by broadly propagating Ca^{2+} waves that are generated at dendritic hot spots, (5) dendritic voltage-gated Na^+ channels, which are functionally inactive in low activity conditions (Hu et al., 2010), start to generate interneuronal ripple oscillations, which are associated with the dendritic Ca^{2+} spikes, and (6) the integration mode of FS-PV INs changes, AP outputs are tightly coupled to the phase of interneuronal ripple oscillations, and the total time-window of AP outputs becomes broader compared to the submillisecond precision in EPSP-AP coupling that characterizes the low activity state.

SPW-R Events Activate Dendritic Hot Spots in FS-PV INs

The main difficulty in imaging hot spot activity in complex dendritic arbors is the inadequate temporal and spatial resolution of currently available imaging technologies, which operate at video-rate time resolution and are constrained to 2D image acquisition in order to maintain an appropriate signal-to-noise ratio. Our fast 3D scanning methods overcome these limitations by providing a high temporal resolution up to tens of microseconds (temporal super-resolution microscopy) (Katona et al., 2012), which allows simultaneous measurement of even the fastest regenerative events in multiple dendritic segments of the thin distal dendritic arborization, with a high spatial discretization on the size scale of dendritic hot spots during SPW-Rs (~4 µm). In order to determine the dendritic active input patterns and underlying ion channel mechanism that are capable of generating the hot spots and the associated dendritic spikes during SPW-Rs, we took advantage of a caged glutamate compound, DNI-Glu•TFA. Its ~7-fold higher uncaging efficiency allowed the more complex spatiotemporal patterns required for this work to be generated: up to 60 active inputs within a short time period (less than one cycle of the ripple oscillation). As phototoxicity increases rapidly and nonlinearly (Ji et al., 2008) as a function of the required laser intensity, the increased uncaging efficiency of DNI-Glu•TFA provides a significant advantage in neurophysiological experiments compared to the widely used MNI-Glu.

These methods yielded several insights into the fine spatiotemporal structure of dendritic hot spot activity. Similar to our previous study in stratum radiatum dendrite-innervating interneurons, here, we have shown that in double-perfused acute slices, the network activity is better preserved and provides spatially and temporally clustered synaptic input patterns to FS-PV INs that activate dendritic hot spots (Chiovini et al., 2010; Katona et al., 2011). In contrast to previous studies in cell cultures where no hot spot activity was found in FS-PV INs (Takahashi et al., 2012), we showed that SPW-R-associated

dendritic hot spots can be intense in FS-PV INs. Moreover, we demonstrated that at a sufficiently high active input number (the second threshold) dendritic Ca^{2+} spikes can emerge from local hot spot activity and can activate long dendritic segments in multiple branches of the apical dendritic tree. Initially, calcium-permeable (~40%) and nonpermeable (~35%) AMPA receptors, and NMDA receptors (~25%) trigger the initial signal in hot spot regions. The second step is for voltage-gated Ca^{2+} and Na^{+} channels to be activated, and propagating dendritic spikes are initiated laterally to the hot spot regions with a significant delay, and spikes then propagate both centripetally and centrifugally dominantly by engaging the available VGCCs (dominantly L-type channels), thereby connecting neighboring hot spots. The VGCCs and Na^{+} channels, which were activated in the second step, also contributed more then 35% to the somatic EPSP amplitude and further increased Ca^{2+} responses in the central hot spot regions. The propagation speed of dendritic Ca^{2+} spikes was relatively low, much slower than the typical AP backpropagation speed, creating dendritic "delay lines" for signal integration. This could provide a relatively broad temporal window for dendritic integration both between and within hot spots, which may play a crucial role in coincidence detection and synaptic plasticity.

Interneuronal Ripple Oscillation as an Ingredient in the Generation of Population Ripple Oscillations

Intrinsic membrane resonances, which are mediated by resonating (e.g., HCN-channels or M-type K^{+} channels) and resonance-amplifying (e.g., persistent Na^{+} channels or NMDA receptors) conductances, have been observed mainly in the relatively low-frequency theta band, with a rapid decrease in amplitude at higher frequencies (Hu et al., 2009; Johnston and Narayanan, 2008; Narayanan and Johnston, 2007; Zemankovics et al., 2010). Earlier studies revealed either no resonance, or a resonance at beta-gamma frequencies in fast-spiking hippocampal interneurons (Zemankovics et al., 2010). The correlated Ca^{2+} responses and electrophysiological data recorded during SPW-Rs have suggested that one unique property of FS-PV INs is that dendritic Ca^{2+} spikes are associated with intrinsically generated membrane potential oscillations in a much higher, ripple-frequency band. Supporting this, clustered input patterns were able to induce interneuronal ripple oscillations in short distal dendritic segments, even when axosomatic Na^{+} channels were blocked. In contrast to VGCCs, Na^{+} channels had a relatively high impact on somatic EPSPs and contributed less to the generation of dendritic Ca^{2+} signals. The dendritic origin of interneuronal ripple oscillations was further supported by the presence of oscillations in dendritic, but not in axosomatic, juxtacellular recordings, and by the weak dependence of the relative oscillation threshold on somatic membrane potential. It is important to note that the detection of interneuronal ripple oscillations was facilitated by the baseline subtraction method which, in contrast to traditional frequency-based approaches (such as band-pass filtering), better preserved the amplitude and the phase of individual oscillation cycles.

The ripple oscillations detected in the membrane voltage of FS-PV INs are actively mediated by Na^{+} channels and may reflect the generation of high-frequency trains of action potentials within the distal apical dendrites. In the presence of interneuronal ripple oscillations, synaptic inputs are related to spike output through the following sequence of events. In the first step, ongoing active inputs are integrated and hot spots are generated. The membrane ripple oscillation starts to form a few millisecond-long time windows for signal integration; finally, after some oscillation periods, the AP output is generated. The AP output is synchronized to these interneuronal ripple oscillations, i.e., EPSPs which are in phase synchrony with the oscillations will be amplified and contribute to the APs. Moreover, an ongoing input assembly (or its failure), may shift the AP phase in a positive (or negative) direction relative to the interneuronal ripple oscillations, forming the firing pattern of individual FS-PV INs in the SPW-R associated cell assembly. Our working hypothesis is that there is a bidirectional relationship between dendritic mechanisms and cell assembly firing: the cell assemblies activate dendritic hot spots, while hot spots generate ripples, which finally determine the neuronal outputs of the individual neurons within cell assemblies. According to this bidirectional relationship, the memory information that is thought to be captured in the hippocampus during SPW-Rs as a temporal pattern of cell assembly discharges (Buzsáki and Silva, 2012) should also be present as dendritic active input patterns with a certain phase relative to the interneuronal ripple oscillations.

In this study, we propose a dendritic hot spot-related mechanism to be integrated into the currently accepted network model of SPW-R activity (Buzsáki and Silva, 2012). According to our results, membrane oscillations at ripple frequencies can be generated following strong depolarizing events in the dendrites of FS-PV INs. In intact hippocampal circuits, this depolarization can be provided predominantly by the synchronized firing of CA3 cell assemblies, which are directly responsible for the envelope of the SPW events (Buzsáki and Silva, 2012). Smaller cell assemblies can also provide the required depolarization, as individual CA3 subfields (Ellender et al., 2010), and CA1 (or CA3) minislices have also been shown to be capable of generating SPW-Rs (Maier et al., 2003, 2011; Nimmrich et al., 2005). Moreover, local application of KCl to the dendritic layer, with a complete blockade of GABAergic and glutamatergic synaptic transmission, reproduced SPW events and was also capable of generating the associated network ripple oscillations in CA1 minisclices (Nimmrich et al., 2005). These data also suggest that a single depolarization event in dendrites without any internal pattern is capable of activating intrinsic membrane mechanisms that then generate the ripple-oscillations. In line with this prediction, we showed that a single activation of clustered glutamatergic inputs in the distal dendrites of FS-PV INs, which generate a depolarizing hump and reproduce the hot spots associated with spontaneous SPW-R events, is also capable of generating secondary membrane oscillations in the ripple frequency range. In summary, we can say that the phase-locked firing during SPW-Rs is not a simple reflection of the discharge pattern of presynaptic cell assemblies, but oscillations can be formed actively and intrinsically by the dendritic membrane.

Although smaller and smaller parts of the hippocampal formation have recently been shown to be possible sources of ripple

oscillations (Buzsáki and Silva, 2012; Ellender et al., 2010; Maier et al., 2003; Nimmrich et al., 2005), ripples have been exclusively considered as a network phenomenon. Here, we demonstrate that the smallest functional unit that can generate fast oscillations in the ripple frequency range when activated by ~30 coincident active inputs is a short (~20 μm) segment of a dendrite, a dendritic hot spot. Although the duration of the interneuronal ripple oscillations increased upon increasing active input number and the onset latency decreased, the oscillation frequency remained stable, suggesting that these dendritic ripple generators are the integrated circuit elements which provide the stable ripple frequency of the network oscillation during SPWs. Interneuronal ripple oscillations could be detected in the local field potential at distances up to a few micrometers from the activated dendritic segments, but whether, and how, these independent dendritic oscillators interact within the dendritic arbor of the same neuron, and throughout the gap-junction-connected dendritic network of interneurons, and how they finally give rise to the local field potential, remains to be investigated.

EXPERIMENTAL PROCEDURES

Mouse Line and Electrophysiology

Horizontal acute brain slices were prepared from transgenic mice expressing eGFP controlled by the parvalbumin promoter (Meyer et al., 2002). Whole-cell recording was performed from FS-PV INs in the CA1 region. In the dual "superfusion" chamber both surfaces of the 450-μm-thick slice were perfused with >10 ml/min (Chiovini et al., 2010; Hájos et al., 2009). LFP (from stratum pyramidale [str. pyr.] of the hippocampal CA1 region) and juxtacellular signals were recorded using glass electrodes (6–9 MΩ) filled with artificial cerebrospinal fluid.

Fast 3D Two-Photon Imaging with Acousto-Optical Scanning

In this study, we improved our 3D-AO imaging and trajectory scanning method (Katona et al., 2012) by increasing the total transmission efficiency at higher wavelengths. Spatial resolution and scanning volume was also increased by ~20% and ~10%, respectively, by optimizing the system for the XLUMPlanFI20×/1.0 objective lens (Olympus, 20×, NA 1.0). Software modules were developed for fast 3D dendritic measurements and to compensate for sample drift.

Preparation of DNI-Glu·TFA and Two-Photon Uncaging

To synthesize DNI-Glu·TFA, we developed a synthetic route. The photochemical yield was measured by comparing response amplitudes as a function of laser intensity in the presence of DNI-Glu·TFA (2.5 mM) and MNI-Glu·TFA (2.5 mM). The shift in response amplitudes indicated a 7.17 ± 0.84-fold higher yield ($p < 0.00001$, $n = 10$) for DNI-Glu·TFA. The uncaging wavelength was set to 740 nm according to the red-shifted two-photon optimum. In simultaneous two-photon uncaging and imaging measurements the Roller Coaster Scanning method was used, as described earlier (Katona et al., 2011).

Data Analysis and Statistics

All neuronal input-output curves could generally be characterized by an initially concave or linear curve (Equation S3 in the Supplemental Experimental Procedures), on top of which a sigmoid-like supralinear increase was superimposed at a given threshold input number (Equation S4 in the Supplemental Experimental Procedures). Threshold input numbers were generally defined as the smallest active input numbers above the sigmoidal increase. Relative fluorescence changes were transformed to Ca^{2+} concentration change using the Equation S5 in the Supplemental Experimental Procedures (Maravall et al., 2000; Rozsa et al., 2004). The statistical difference was measured using the Student's t test (*, **, or *** indicate p values of less than 0.05, 0.01, or 0.001, respectively). If not otherwise indicated, data are presented as means ± SEM.

Compartmental Modeling

Simulations were performed using a detailed compartmental model of a PV+ CA1 basket cell, based on a morphological reconstruction (Gulyás et al., 1999). Passive parameters were uniform throughout the cell. The model neuron contained transient Na^+, delayed-rectifier type K^+, and high-voltage-activated, slowly inactivating Ca^{2+} channels, which were described by a standard Hodgkin-Huxley formalism and were distributed nonuniformly (see Equations S6–S25 in the Supplemental Experimental Procedures). Synaptic input was modeled as a conductance change with a biexponential time course. Simulations were run in the Neuron simulation environment (Carnevale and Hines, 2006).

Baseline Subtraction Method

Band-pass filtering can generate extra oscillation events and phase shifts when the filtered oscillations are irregular, which is the case for SPW-associated ripple oscillations (Figure S2). To avoid these errors, in the first step we used Gauss filtering (100 Hz) on the raw traces to generate a "baseline," which was then subtracted from the raw traces (referred to as baseline-subtraction method, Figure S2A) to better preserve the amplitude and phase of the individual ripple oscillation cycles (Figure S2).

See Supplemental Experimental Procedures for a detailed description of the Experimental Procedures.

SUPPLEMENTAL INFORMATION

Supplemental Information includes Supplemental Experimental Procedures, seven figures, two tables, and four movies and can be found with this article online at http://dx.doi.org/10.1016/j.neuron.2014.04.004.

AUTHOR CONTRIBUTIONS

Optical design was performed by P.M., G. Szalay, and B.R. Software was written by G.K. In vitro measurements were performed by B.C., F.G.T., D.P., Z.S., and A.K. Analysis was carried out by B.R., B.C., F.G.T., and D.P. Modeling was performed by S.K., and M.F.S. Animals were provided by G. Szabó. This manuscript was written by B.R., B.C., F.G.T., and S.K. with comments from all authors. B.R. supervised the project.

ACKNOWLEDGMENTS

We thank György Buzsáki, Botond Roska, Zoltán Nusser, Mark Eyre, Noémi Holderith, and Szabolcs Oláh for their helpful comments. This work was supported by a Hungarian-French (TÉT_0389), GOP-1.1.1, Swiss-Hungarian SH/7/2/8, KMR_0214, OTKA (K83251, K105997), FP7-ICT-604102-HBP, Magyary Zoltán (13-0314), TÁMOP-4.2.1. B-11/2/KMR-2011-0002, and ERC-2011-ADG-294313 grants. G.K. and B.R. are founders of Femtonics Kft. B.R. is a member of its scientific advisory board.

Accepted: March 18, 2014
Published: May 21, 2014

REFERENCES

Abrahamsson, T., Cathala, L., Matsui, K., Shigemoto, R., and Digregorio, D.A. (2012). Thin dendrites of cerebellar interneurons confer sublinear synaptic integration and a gradient of short-term plasticity. Neuron *73*, 1159–1172.

Ali, A.B., Deuchars, J., Pawelzik, H., and Thomson, A.M. (1998). CA1 pyramidal to basket and bistratified cell EPSPs: dual intracellular recordings in rat hippocampal slices. J. Physiol. *507*, 201–217.

Avermann, M., Tomm, C., Mateo, C., Gerstner, W., and Petersen, C.C. (2012). Microcircuits of excitatory and inhibitory neurons in layer 2/3 of mouse barrel cortex. J. Neurophysiol. *107*, 3116–3134.

Bähner, F., Weiss, E.K., Birke, G., Maier, N., Schmitz, D., Rudolph, U., Frotscher, M., Traub, R.D., Both, M., and Draguhn, A. (2011). Cellular correlate

of assembly formation in oscillating hippocampal networks in vitro. Proc. Natl. Acad. Sci. USA *108*, E607–E616.

Buhl, E.H., Szilágyi, T., Halasy, K., and Somogyi, P. (1996). Physiological properties of anatomically identified basket and bistratified cells in the CA1 area of the rat hippocampus in vitro. Hippocampus *6*, 294–305.

Buzsáki, G. (1986). Hippocampal sharp waves: their origin and significance. Brain Res. *398*, 242–252.

Buzsáki, G. (2010). Neural syntax: cell assemblies, synapsembles, and readers. Neuron *68*, 362–385.

Buzsáki, G., and Chrobak, J.J. (2005). Synaptic plasticity and self-organization in the hippocampus. Nat. Neurosci. *8*, 1418–1420.

Buzsáki, G., and Silva, F.L. (2012). High frequency oscillations in the intact brain. Prog. Neurobiol. *98*, 241–249.

Carnevale, N.T., and Hines, M.L. (2006). The NEURON Book. (New York: Cambridge University Press).

Chiovini, B., Turi, G.F., Katona, G., Kaszás, A., Erdélyi, F., Szabó, G., Monyer, H., Csákányi, A., Vizi, E.S., and Rózsa, B. (2010). Enhanced dendritic action potential backpropagation in parvalbumin-positive basket cells during sharp wave activity. Neurochem. Res. *35*, 2086–2095.

Ellender, T.J., Nissen, W., Colgin, L.L., Mann, E.O., and Paulsen, O. (2010). Priming of hippocampal population bursts by individual perisomatic-targeting interneurons. J. Neurosci. *30*, 5979–5991.

Fricker, D., and Miles, R. (2000). EPSP amplification and the precision of spike timing in hippocampal neurons. Neuron *28*, 559–569.

Girardeau, G., Benchenane, K., Wiener, S.I., Buzsáki, G., and Zugaro, M.B. (2009). Selective suppression of hippocampal ripples impairs spatial memory. Nat. Neurosci. *12*, 1222–1223.

Glickfeld, L.L., and Scanziani, M. (2006). Distinct timing in the activity of cannabinoid-sensitive and cannabinoid-insensitive basket cells. Nat. Neurosci. *9*, 807–815.

Goldberg, J.H., and Yuste, R. (2005). Space matters: local and global dendritic Ca2+ compartmentalization in cortical interneurons. Trends Neurosci. *28*, 158–167.

Goldberg, J.H., Tamas, G., Aronov, D., and Yuste, R. (2003a). Calcium microdomains in aspiny dendrites. Neuron *40*, 807–821.

Goldberg, J.H., Tamas, G., and Yuste, R. (2003b). Ca2+ imaging of mouse neocortical interneurone dendrites: Ia-type K+ channels control action potential backpropagation. J. Physiol. *551*, 49–65.

Goldberg, J.H., Yuste, R., and Tamas, G. (2003c). Ca2+ imaging of mouse neocortical interneurone dendrites: contribution of Ca2+-permeable AMPA and NMDA receptors to subthreshold Ca2+dynamics. J. Physiol. *551*, 67–78.

Gulyás, A.I., Miles, R., Sík, A., Tóth, K., Tamamaki, N., and Freund, T.F. (1993). Hippocampal pyramidal cells excite inhibitory neurons through a single release site. Nature *366*, 683–687.

Gulyás, A.I., Megías, M., Emri, Z., and Freund, T.F. (1999). Total number and ratio of excitatory and inhibitory synapses converging onto single interneurons of different types in the CA1 area of the rat hippocampus. J. Neurosci. *19*, 10082–10097.

Hájos, N., Ellender, T.J., Zemankovics, R., Mann, E.O., Exley, R., Cragg, S.J., Freund, T.F., and Paulsen, O. (2009). Maintaining network activity in submerged hippocampal slices: importance of oxygen supply. Eur. J. Neurosci. *29*, 319–327.

Hu, H., Vervaeke, K., Graham, L.J., and Storm, J.F. (2009). Complementary theta resonance filtering by two spatially segregated mechanisms in CA1 hippocampal pyramidal neurons. J. Neurosci. *29*, 14472–14483.

Hu, H., Martina, M., and Jonas, P. (2010). Dendritic mechanisms underlying rapid synaptic activation of fast-spiking hippocampal interneurons. Science *327*, 52–58.

Ji, N., Magee, J.C., and Betzig, E. (2008). High-speed, low-photodamage nonlinear imaging using passive pulse splitters. Nat. Methods *5*, 197–202.

Johnston, D., and Narayanan, R. (2008). Active dendrites: colorful wings of the mysterious butterflies. Trends Neurosci. *31*, 309–316.

Katona, G., Kaszás, A., Turi, G.F., Hájos, N., Tamás, G., Vizi, E.S., and Rózsa, B. (2011). Roller Coaster Scanning reveals spontaneous triggering of dendritic spikes in CA1 interneurons. Proc. Natl. Acad. Sci. USA *108*, 2148–2153.

Katona, G., Szalay, G., Maák, P., Kaszás, A., Veress, M., Hillier, D., Chiovini, B., Vizi, E.S., Roska, B., and Rózsa, B. (2012). Fast two-photon in vivo imaging with three-dimensional random-access scanning in large tissue volumes. Nat. Methods *9*, 201–208.

Klausberger, T., Magill, P.J., Márton, L.F., Roberts, J.D., Cobden, P.M., Buzsáki, G., and Somogyi, P. (2003). Brain-state- and cell-type-specific firing of hippocampal interneurons in vivo. Nature *421*, 844–848.

Kleindienst, T., Winnubst, J., Roth-Alpermann, C., Bonhoeffer, T., and Lohmann, C. (2011). Activity-dependent clustering of functional synaptic inputs on developing hippocampal dendrites. Neuron *72*, 1012–1024.

Lamsa, K.P., Heeroma, J.H., Somogyi, P., Rusakov, D.A., and Kullmann, D.M. (2007). Anti-Hebbian long-term potentiation in the hippocampal feedback inhibitory circuit. Science *315*, 1262–1266.

Lapray, D., Lasztoczi, B., Lagler, M., Viney, T.J., Katona, L., Valenti, O., Hartwich, K., Borhegyi, Z., Somogyi, P., and Klausberger, T. (2012). Behavior-dependent specialization of identified hippocampal interneurons. Nat. Neurosci. *15*, 1265–1271.

Larkum, M.E., Nevian, T., Sandler, M., Polsky, A., and Schiller, J. (2009). Synaptic integration in tuft dendrites of layer 5 pyramidal neurons: a new unifying principle. Science *325*, 756–760.

Lorenz, A., Osman, F., Sun, W., Nandi, S., Steinacher, R., and Whitby, M.C. (2012). The fission yeast FANCM ortholog directs non-crossover recombination during meiosis. Science *336*, 1585–1588.

Losonczy, A., and Magee, J.C. (2006). Integrative properties of radial oblique dendrites in hippocampal CA1 pyramidal neurons. Neuron *50*, 291–307.

Maier, N., Nimmrich, V., and Draguhn, A. (2003). Cellular and network mechanisms underlying spontaneous sharp wave-ripple complexes in mouse hippocampal slices. J. Physiol. *550*, 873–887.

Maier, N., Tejero-Cantero, A., Dorrn, A.L., Winterer, J., Beed, P.S., Morris, G., Kempter, R., Poulet, J.F., Leibold, C., and Schmitz, D. (2011). Coherent phasic excitation during hippocampal ripples. Neuron *72*, 137–152.

Makino, H., and Malinow, R. (2011). Compartmentalized versus global synaptic plasticity on dendrites controlled by experience. Neuron *72*, 1001–1011.

Maravall, M., Mainen, Z.F., Sabatini, B.L., and Svoboda, K. (2000). Estimating intracellular calcium concentrations and buffering without wavelength ratioing. Biophys. J. *78*, 2655–2667.

Meyer, A.H., Katona, I., Blatow, M., Rozov, A., and Monyer, H. (2002). In vivo labeling of parvalbumin-positive interneurons and analysis of electrical coupling in identified neurons. J. Neurosci. *22*, 7055–7064.

Narayanan, R., and Johnston, D. (2007). Long-term potentiation in rat hippocampal neurons is accompanied by spatially widespread changes in intrinsic oscillatory dynamics and excitability. Neuron *56*, 1061–1075.

Nimmrich, V., Maier, N., Schmitz, D., and Draguhn, A. (2005). Induced sharp wave-ripple complexes in the absence of synaptic inhibition in mouse hippocampal slices. J. Physiol. *563*, 663–670.

Nörenberg, A., Hu, H., Vida, I., Bartos, M., and Jonas, P. (2010). Distinct nonuniform cable properties optimize rapid and efficient activation of fast-spiking GABAergic interneurons. Proc. Natl. Acad. Sci. USA *107*, 894–899.

Polsky, A., Mel, B.W., and Schiller, J. (2004). Computational subunits in thin dendrites of pyramidal cells. Nat. Neurosci. *7*, 621–627.

Pouille, F., and Scanziani, M. (2004). Routing of spike series by dynamic circuits in the hippocampus. Nature *429*, 717–723.

Rozsa, B., Zelles, T., Vizi, E.S., and Lendvai, B. (2004). Distance-dependent scaling of calcium transients evoked by backpropagating spikes and synaptic activity in dendrites of hippocampal interneurons. J. Neurosci. *24*, 661–670.

Schiller, J., Major, G., Koester, H.J., and Schiller, Y. (2000). NMDA spikes in basal dendrites of cortical pyramidal neurons. Nature *404*, 285–289.

Sohal, V.S., Zhang, F., Yizhar, O., and Deisseroth, K. (2009). Parvalbumin neurons and gamma rhythms enhance cortical circuit performance. Nature *459*, 698–702.

Stuart, G., Spruston, N., and Hausser, M. (1999). Dendrites, Second Edition. (Oxford: Oxford University Press).

Takahashi, N., Kitamura, K., Matsuo, N., Mayford, M., Kano, M., Matsuki, N., and Ikegaya, Y. (2012). Locally synchronized synaptic inputs. Science *335*, 353–356.

Taxidis, J., Coombes, S., Mason, R., and Owen, M.R. (2012). Modeling sharp wave-ripple complexes through a CA3-CA1 network model with chemical synapses. Hippocampus *22*, 995–1017.

Topolnik, L. (2012). Dendritic calcium mechanisms and long-term potentiation in cortical inhibitory interneurons. Eur. J. Neurosci. *35*, 496–506.

Traub, R.D., and Bibbig, A. (2000). A model of high-frequency ripples in the hippocampus based on synaptic coupling plus axon-axon gap junctions between pyramidal neurons. J. Neurosci. *20*, 2086–2093.

Tukker, J.J., Lasztóczi, B., Katona, L., Roberts, J.D., Pissadaki, E.K., Dalezios, Y., Márton, L., Zhang, L., Klausberger, T., and Somogyi, P. (2013). Distinct dendritic arborization and in vivo firing patterns of parvalbumin-expressing basket cells in the hippocampal area CA3. J. Neurosci. *33*, 6809–6825.

Vervaeke, K., Lorincz, A., Nusser, Z., and Silver, R.A. (2012). Gap junctions compensate for sublinear dendritic integration in an inhibitory network. Science *335*, 1624–1628.

Vinet, J., and Sík, A. (2006). Expression pattern of voltage-dependent calcium channel subunits in hippocampal inhibitory neurons in mice. Neuroscience *143*, 189–212.

Zemankovics, R., Káli, S., Paulsen, O., Freund, T.F., and Hájos, N. (2010). Differences in subthreshold resonance of hippocampal pyramidal cells and interneurons: the role of h-current and passive membrane characteristics. J. Physiol. *588*, 2109–2132.